

UC Riverside

UC Riverside Previously Published Works

Title

Colocalization of protein and microRNA markers reveals unique extracellular vesicle subpopulations for early cancer detection.

Permalink

<https://escholarship.org/uc/item/0b2773km>

Journal

Science Advances, 10(9)

Authors

Li, Zongbo

Guo, Kaizhu

Gao, Ziting

et al.

Publication Date

2024-03-01

DOI

10.1126/sciadv.adh8689

Peer reviewed

CANCER

Colocalization of protein and microRNA markers reveals unique extracellular vesicle subpopulations for early cancer detection

Zongbo Li^{1†}, Kaizhu Guo^{1†}, Ziting Gao¹, Junyi Chen², Zuyang Ye¹, Minghui Cao³, Shizhen Emily Wang³, Yadong Yin¹, Wenwan Zhong^{1,2*}

Extracellular vesicles (EVs) play important roles in cell-cell communication but are highly heterogeneous, and each vesicle has dimensions smaller than 200 nm with very limited amounts of cargos encapsulated. The technique of NanOstirBar (NOB)–EnabLed Single Particle Analysis (NOBEL-SPA) reported in the present work permits rapid inspection of single EV with high confidence by confocal fluorescence microscopy, thus enables colocalization assessment for selected protein and microRNA (miRNA) markers in the EVs produced by various cell lines, or present in clinical sera samples. EV subpopulations marked by the colocalization of unique protein and miRNA combinations were discovered to be able to detect early-stage (stage I or II) breast cancer (BC). NOBEL-SPA can be adapted to analyze other types of cargo molecules or other small submicron biological particles. Study of the sorting of specific cargos to heterogeneous vesicles under different physiological conditions can help discover distinct vesicle subpopulations valuable in clinical examination and therapeutics development and gain better understanding of their biogenesis.

INTRODUCTION

Extracellular vesicles (EVs) secreted by cells can mediate cell-cell communication (1–5) and are present in all biological fluids (6, 7), easily accessible with minimal invasion (8). They are classified into different subtypes; (9–15) and the two smaller (diameter, ~40 to 250 nm) subtypes called exosomes and microvesicles have attracted great attention in biomedical research because of their unique biogenesis pathways and diverse types of cargo molecules (1–3, 5, 16). EVs have been associated with immune responses, viral pathogenicity, cancer progression, and cardiovascular or central nervous system-related diseases (17–20), supporting their high potential as diagnostic and therapeutic tools. However, it is very challenging to identify the disease-related EVs. They are highly heterogeneous, different in their sizes, contents, cells of origin, biogenesis pathways, and functional impacts on recipient cells (21–23). While the total EV concentration in the peripheral circulation can reach 10^9 vesicles/ml (24), the unique EV subpopulations that carry out specific disease-related functions or are derived from cells undergoing pathological transition (21, 25) could be at very low abundance during the early development stage (26). It has been projected mathematically that, for bulk detection, it would need techniques sensitive enough to accommodate an EV input of ~100 EV particles/ml to detect those released by small human tumors ($<1 \text{ cm}^3$), which are curable if caught early (27, 28). Such a sensitivity requirement is very difficult if not impossible to be met by the conventional methods of enzyme-linked immunosorbent assay (ELISA), Western blotting (WB), and bead-based flow cytometry (FCM). In addition, bulk analysis only produces the ensemble average of the varying signals from a swarm of heterogeneous EVs and very likely misses the signals from the distinct subpopulations present at trace levels.

To simultaneously overcome the heterogeneity and sensitivity issues in EV analysis, pioneering works analyzed single EVs using high-resolution FCM (29–32), super-resolution microscopy (33, 34), and droplet-based next generation sequencing (35). Confocal fluorescence microscopy (CFM) or total internal reflection fluorescence microscopy has also come to the spot light of single EV analysis because of their relatively lower cost in instrumentation and less complex operation while offering direct visualization of the vesicles (28, 36, 37). As listed in table S1, the most state-of-the-art developments using fluorescence microscopy detected either proteins or nuclei acids on single EVs, confirming the presence of EV subpopulations bearing different phenotypic features and their premises in marking disease development (28, 38–42). Still, single EV analysis is very difficult, owing to their extremely small sizes and the low amounts of cargos enclosed in each EV. While impressive detection performance has been obtained with the pioneering developments, assay turnaround time, limit of detection (LOD), and sample consumption are yet to be improved to meet the needs in early detection and frequent disease monitoring (38–42). Single EV capture was only achieved with specially designed surface features fabricated on microfluidic devices or by controlling a large bead-to-EV molar ratio, which is not easy to do when testing unknown samples. Simultaneously analyzing multiple types of cargos in single EVs with comparable sensitivity as protein detection has not yet been achieved either (43).

Among the diverse EV cargos, noncoding RNAs, particularly microRNAs (miRNAs), have been widely revealed for their potential to modulate the biological functions of recipient cells and contribute to cell proliferation, angiogenesis, metastasis, and drug resistance (44–46). Proteins have also been found to be indicative of the physiological conditions of the cells of origin and deeply involved in EV biogenesis, uptake, and intracellular signaling (8, 47–50). Because of their important roles played in EV functions relevant to disease development, we hypothesize that simultaneously detecting the protein and miRNA cargos on single EVs can greatly improve the specificity and efficiency in using EVs for disease detection (28). In addition, colocalization of proteins and miRNAs on the

Copyright © 2024 The Authors, some rights reserved; exclusive licensee American Association for the Advancement of Science. No claim to original U.S. Government Works. Distributed under a Creative Commons Attribution NonCommercial License 4.0 (CC BY-NC).

¹Department of Chemistry, University of California-Riverside, Riverside, CA 92521, USA. ²Environmental Toxicology Graduate Program, University of California-Riverside, Riverside, CA 92521, USA. ³Department of Pathology, University of California-San Diego, La Jolla, CA 92093, USA.

*Corresponding author. Email: wenwan.zhong@ucr.edu

†These authors contributed equally to this work.

same EV can also assist with study of the sorting mechanisms of miRNAs into different EV subpopulations (51–53). Here, we report the technique of NanOstirBar (NOB)–EnabLed Single Particle Analysis (NOBEL-SPA) that uses the multifunctional NOBs to enable detection of both the protein and miRNA cargos on single EVs. The NOBs not only act as regular magnetic particles to facilitate easy handling but also can spin freely in the rotating magnetic field to speed up molecular diffusion to their surface and prompt rapid target binding and thorough removal of the nonspecifically adsorbed molecules. Moreover, each NOB has comparable dimensions as the single EV. Thus, it can easily realize one-NOB-one-vesicle during EV capture and then act as an isolated “island” for immobilization of the individual EV and its cargo molecules, preventing EV aggregation and diffusion of the intravesicular molecules once the membrane structure is destroyed. Our study tested selective protein (CD24, CD44, HER2, EGFR, and MUC1) and miRNA (miR-21, miR-122, miR-155, and let-7a) markers. The up-regulation of CD44, HER2, EGFR, and MUC1 has been widely reported in breast cancer (BC) cells and tissues and in the EVs isolated from patients with BC (54–58); and the miRNA targets also can regulate proliferation, migration, and invasion of BC cells (59, 60). The few marker molecules concentrated on each NOB can be illuminated by the DNA nanoflowers (DNF) grown from rolling circle amplification (RCA) (58, 61), making the single EV carrying specific markers easily detected with high confidence by the diffraction-limited confocal fluorescence microscopy. NOBEL-SPA was applied to analyze the presence and colocalization of a selection

of protein and miRNA markers in the exosomes produced by various tumor cell lines or present in the sera samples collected from patients with BC. Distinct EV subpopulations defined by the colocalization of specific tumor miRNA and protein markers were found to be able to differentiate EVs by their cells of origin and to differentiate patients with BC from healthy controls, with some even showing significant differences between healthy controls, stage I, and stage II BC patients.

RESULTS

NOBs to facilitate single EV counting and yield efficient EV capture

The previous works for using microscopy to analyze single EVs typically captured the EVs on flat glass surface for imaging (28, 36, 38, 40, 41, 58, 61), which could be slow and inefficient due to the slow kinetics in surface diffusion. In addition, EVs aggregate easily, preventing accurate recognition of individual vesicles. In the present work, we discovered that the superparamagnetic, silica-coated nanorods (62) can be used to enable single EV analysis (Fig. 1A). While the NOBs are small and can be homogeneously dispersed in aqueous solutions, complete pull-down from a 1.5-ml solution by a magnet can be done in 10 s. They also can spin in solution if driven by a low-gradient rotating magnetic field generated by a stirrer plate. We synthesized the NOBs with the dimension of ~150 nm by 50 nm and modified their silica surface with carboxyl groups (fig. S1). This type of modification was chosen because they can be easily

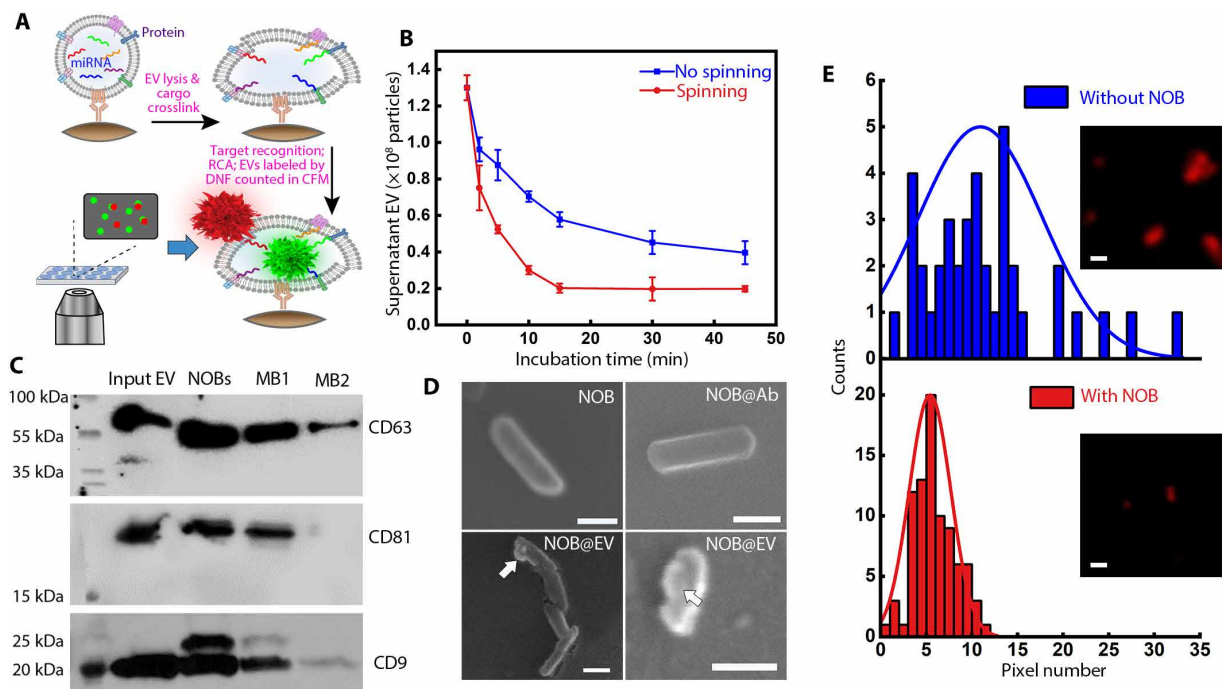


Fig. 1. NOB to facilitate single vesicle analysis. (A) Scheme of NOBEL-SPA. (B) Plot of EV numbers remained in the supernatant after incubation with NOB_{Exc} for various durations as detected by NTA. Value and error bars are the average and SD of three repeated measurements. (C) WB results for detection of CD63, CD81, and CD9 in the starting solution and in the EVs pulled down by NOB_{Exc} or by MBs with diameter around 1 (MB1) or 0.22 μ m (MB2) which were conjugated with the same antibody mixture as NOB_{Exc} after 30-min incubation. The first lane was from a protein ladder. (D) SEM images of the individual NOB, NOB_{Exc}, and NOB_{Exc} with the bound EV (pointed by the arrows). Scale bars, 100 nm. (E) Histograms for the pixel numbers of the fluorescent particles detected after EV lysis and cargo crosslinking, with the EVs captured on the glass slide surface (without NOB) or by NOB_{Exc} (with NOB). The inset images: 10 μ m by 10 μ m. Scale bars, 1 μ m.

conjugated to proteins with primary amines on surface via carbodiimide chemistry, and their negative charges could help repel the matrix components in biospecimens like serum to reduce detection background. Then, we conjugated the NOBs with the mixture of antibodies against the exosomal markers of CD63/CD9/CD81, which was referred as NOB_{Exo} in the following text, and evaluated their capability in capturing EVs from a pure sample purchased commercially.

First, we assessed the number of EVs remained in the supernatant after removing the NOB_{Exo} at various incubation times with the EV sample by nanoparticle tracking analysis (NTA). We found that, with spinning, the NOB_{Exo} caused a much faster decrease of the EV number in the supernatant, compared to the no-spinning condition, and reached the minimum in 15 min, which was two times lower than that from 45-min incubation with no spinning (Fig. 1B). Spinning the NOBs can also help reduce nonspecific adsorption during wash and produced lower background signals than that attained by the wash condition without spinning (fig. S2). In addition, much more exosomal markers of CD63, CD81, and CD9 were pulled down by the spinning NOB_{Exo} than by the spherical magnetic beads (MBs) conjugated with the same antibody mixture, as found by WB (Fig. 1C). All three cases used the same EV input and same particle total mass. The gel images show that the amounts of the CD proteins isolated by NOB_{Exo} were almost comparable to those present in the starting solution, supporting >90% recovery. Using ELISA and NTA to quantify the CD proteins and EV particles, respectively, remained in the supernatant after EV immunoprecipitation by these three types of nanoparticles also confirmed the higher capture efficiency attained by NOB_{Exo} than the MBs (fig. S3). These results well support that the NOBs outperform the spherical particles in EV immuno-capture, and their spinning feature should be a vital contributor to this superior capability, probably by promoting molecular diffusion to the NOB surface to facilitate fast specific binding and thorough removal of the weakly bound impurities.

NOBs to enable miRNA detection in single vesicle

Besides rapid and efficient EV capture, NOBs can simplify single EV counting and facilitate analysis of the intravesicular cargos like miRNAs. Since the NOBs have the dimensions comparable to those of the EVs, each NOB can capture only few EVs due to space hindrance. We further limited the number of EVs captured per NOB_{Exo} by using a molar ratio of 1:10 for NOB: antibody in the conjugation. We can see from the scanning electron microscopy (SEM) images shown in Fig. 1D (also fig. S4) that either no or just one EV was found on each NOB_{Exo}. With the individual EVs spatially confined and separated from each other with minimized aggregation, counting the single EVs illuminated by the fluorescent DNF in CFM is highly simplified. The NOBs also provide the solid support for fixing the EVs and their cargos upon the EV membrane structures broken down by detergents, allowing the analysis of intravesicular miRNAs (Fig. 1A). We lysed the exosomes captured by NOB_{Exo} via a 10-min treatment of 4% paraformaldehyde (PFA) (63) and used 1-ethyl-3-(3-dimethylaminopropyl) carbodiimide (EDC) to cross-link the 5'-phosphate of RNA (64) to the EV proteins and antibodies on the NOBs (fig. S5). PFA should expose the enclosed miRNAs, and crosslinking could prevent miRNAs from diffusing to the surrounding area and preserve the high initial concentrations of the miRNAs within each vesicle. Then, the exposed miRNAs hybridize with the hairpin probe that carries a complementary sequence to the

target miRNA and a primer region for binding with the circular template to initiate RCA (fig. S6). The sequence of RCA product permits self-hybridization to fold into a nanostructure and attachment of numerous fluorophores (58, 61). The DNF-labeled EV supported by a NOB can be imaged as a bright fluorescent particle. The sizes of the fluorescence particles resulted from the NOB-captured EVs were much smaller (occupying only 4 to 8 imaging pixels) and more homogeneous (showing a narrower distribution profile of the pixel numbers per particle) compared to those not supported by the NOBs (Fig. 1E). A size of 4 to 8 pixels under our imaging condition is equivalent to a dimension of ~250 to 300 nm, matching well with that of the single EV labeled with the DNS as found in our previous works (58, 61).

We carried out NOBEL-SPA for detection of two potential tumor miRNA markers, miR-155 and miR-122, in the EV standards, using NOB_{Exo} for EV isolation. Good detection specificity using the hairpin probes was confirmed: Only the target miRNA (miR-155 or miR-122) yielded positive RCA reaction with the corresponding hairpin probe but not other miRNAs nor the single-stranded RNA with a sequence 1- or 2-nucleotide different from the target strand at various locations (figs. S6 to S8). We stained the EVs with DiB and labeled the DNF grown upon recognition of miR-155 or miR-122 with Alexa 633 (λ_{ex} 621 nm/ λ_{em} 639 nm) (Fig. 2A). Although the fluorescence intensity of the DNF should reflect the miRNA quantity enclosed in each EV, the DNF resulted from RCA could have varied lengths and labeled by different number of fluorophores, which could also contribute to intensity variation. Similarly, membrane staining may not be homogeneous across all vesicles. Thus, in the present work, we chose to use the counts of EVs exhibiting above-the-threshold fluorescent signals originated from membrane staining or miRNA-initiated DNF growth for evaluation of the EV as well as EV miRNA contents in our samples but not the fluorescence intensity found on each vesicle. A similar approach has also been adopted in other single EV analysis techniques (65).

The number of the stained EVs, P_{EV} , and that of the DNF-labeled EVs, P_{miRNA} , detected by CFM were both linearly proportional to the input concentration in the range of 200 to 10^5 EV particles/ μ l (P/μ l) (sample volume = 10 μ l) when plotted in the log scales (solid lines in Fig. 2B). If we blocked the target miRNA by a complementary single-stranded DNA (ssDNA) before the addition of the hairpin probe, then no DNF-labeled EV was detected by CFM (fig. S9). Using the 3σ method, we calculated the LOD for detection of the stained EVs, or the EV miRNA, i.e., miR-155 and miR-122, being 4, 3.1, and 18 P/μ l, respectively (figs. S7 and S8). These LODs are lower than those previously reported for EV surface protein (58) and miRNAs in single EVs (41, 66), owing to the high EV capture efficiency and the effective preservation of the EV cargos on NOB. The LOD differences between the two miRNAs reflect the differential loading of these two miRNAs in this EV sample: Using the miRNA quantity obtained from reverse transcription polymerase chain reaction (RT-PCR) and the EV counts measured by NTA, we calculated that averagely at least three copies of miR-155 were encapsulated in each EV; but only ~2 copies of miR-122 were present in ~100 EVs (fig. S11).

We found that, in the same EV sample, the ratio of P_{miRNA}/P_{EV} for the same miRNA did not change substantially with different EV inputs (dashed lines in Fig. 2B) but were distinct between two miRNAs: While the typical P_{miRNA}/P_{EV} value was ~60% for miR-155, that for the low-abundant miR-122 was only ~20%. We then designed

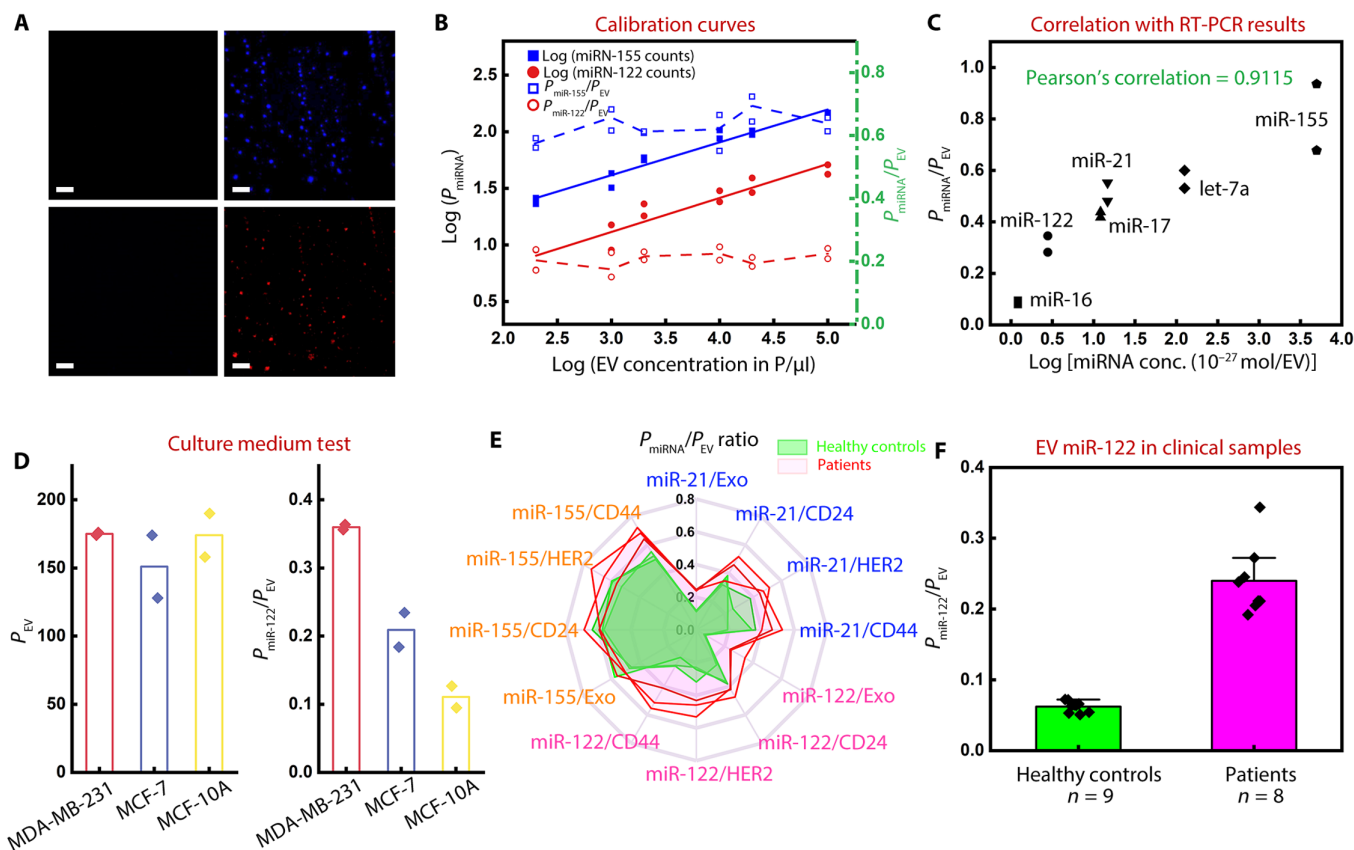


Fig. 2. NOBEL-SPA for analysis of EV miRNAs associated with individual EVs. (A) Representative images of the DiB-stained EVs captured by NOB (top) and illuminated by the DNF labels for miR-155 detection (bottom) collected with no (left) or 2×10^5 P/ μ l (right) EVs. Scale bars, 10 μ m. (B) Plots of $\log(P_{\text{miRNA}} \text{ counts})$ (solid lines) or $P_{\text{miRNA}}/P_{\text{EV}}$ ratio (dashed lines) versus $\log(\text{EV concentration in P}/\mu\text{l})$ for miR-155 (blue) and miR-122 (red). (C) Correlation between $P_{\text{miRNA}}/P_{\text{EV}}$ ratios ($n = 2$) detected by NOBEL-SPA and $\log(\text{miRNA amount per vesicle})$ detected by RT-PCR and NTA for various miRNAs. (D) P_{EV} and $P_{\text{miR-122}}/P_{\text{EV}}$ ($n = 2$) detected in the culture medium from MCF-10A, MCF-7, and MDA-MB-231 cells after 48 hours EV harvest. The NOBs uses in (A) to (D) were NOB_{Exo}. (E) Spider web plot comparing the ratios of $P_{\text{miRNA}}/P_{\text{EV}}$ obtained in the sera of three patients with BC (pink) and three healthy controls (green), with the EVs captured by NOB_{Exo} or NOBs conjugated with the antibody targeting the surface protein of HER2 (NOB_{HER2}), CD44 (NOB_{CD44}), or CD24 (NOB_{CD24}) and respectively detecting the EV-associated miR-155, miR-21, or miR-122. (F) The ratio of $P_{\text{miRNA}}/P_{\text{EV}}$ found in the sera of eight patients with BC (magenta columns) and nine healthy controls (green columns), with the exosomes captured by NOB_{Exo} and detecting the exosomal miR-122. Each data point displayed in (C) to (F) was the average value found in 10 images taken for each sample.

specific hairpin probes for various miRNAs (figs. S10 and S11) and confirmed that indeed the $P_{\text{miRNA}}/P_{\text{EV}}$ ratio varied among different miRNAs and was positively correlated ($R^2 = 0.9115$) with the $\log(\text{moles of miRNA per particle})$ values obtained by quantifying each miRNA in 10^8 EV particles by RT-PCR (Fig. 2C and fig. S11). These results prove that the $P_{\text{miRNA}}/P_{\text{EV}}$ ratio is reflective to the abundance of EV miRNAs in the sample, allowing NOBEL-SPA to accurately compare the miRNA expression levels in different EV samples without the need to quantify the total EVs or total EV RNAs. Our method requires an input of <2000 EV particles, while RT-PCR needs $>10^7$ particles for quantification of EV miRNA and is much more efficient and faster than RT-PCR by working with unprocessed samples with no need of RNA extraction.

Moreover, we subjected three representative EV samples to ribonuclease (RNase) treatment: the purchased pure EVs, the EVs harvested from the culture medium of MDA-MB-231 and precipitated by ultracentrifugation, and those present in pooled human serum without going through any sedimentation process. RNase treatment should digest any RNA adsorbed on EV surface but not protected by the membrane structure. However, such treatment did

not bring in statistically significant difference in the $P_{\text{miRNA}}/P_{\text{EV}}$ ratios obtained by NOBEL-SPA in these samples for all of the four miRNAs tested (miR-155, miR-122, miR-21, and let-7a) (figs. S12 to S14). We also can see from fig. S5 that a much lower particle count would be obtained by labeling the EVs with DNF if the EV sample was not treated by PFA to break down the membrane structures. These results prove that our method indeed detects the EV-enclosed miRNAs but not those adsorbed on EV surface.

Differential loading of miRNAs in EVs from different sources

The high sensitivity and simplicity of NOBEL-SPA permit quick assessment of EV production from cells and the enclosed miRNA contents. To illustrate this capability, we sampled 5 μ l of culture medium of MCF-10A (nontumor), MCF-7 (low metastatic tumor), and MDA-MB-231 (metastatic tumor) cells at various time points (0 to 48 hours) during EV harvest and tested the contents of EVs and EV miR-122 in these samples by isolating and imaging the EVs by NOB_{Exo}. We found that the number of EVs isolated by NOB_{Exo}, i.e., P_{EV} , steadily increased with the harvest time but exhibited no difference in the rate of increase nor in the number of total EVs among

the three cell lines (Fig. 2D and fig. S15). On the other hand, while the number of the miR-122⁺ EV particles, i.e., P_{miRNA} , also increased with the harvest time for all three cell lines, the increase rates were different, leading to significantly different $P_{\text{miRNA}}/P_{\text{EV}}$ ratios collected at 48 hours (Fig. 2D): the EVs from MDA-MB-231 exhibiting the highest ratio, which is more than three times larger than that of the EVs from MCF-10A, which displayed the lowest $P_{\text{miRNA}}/P_{\text{EV}}$ value. Because all the EVs pulled down by NOB_{Exo} should be exosomes, this result agrees with the previous findings on the specific loading of miR-122 in the exosomes from metastasis BC cell lines like MDA-MB-231 (44, 45, 53).

The three cell lines tested above are widely studied to advance understanding of the biology of BCs (67, 68). Thus, we further applied our technique to analyze the EVs and their miRNA contents present in human sera collected from patients with BC and healthy controls. We captured the EVs by NOB_{Exo} or by the NOBs conjugated to the antibody against CD44, CD24, or HER2, proteins reported to be up-regulated in BC cells or tissues and explored the loading of various tumor miRNAs (miR-21, miR-122, and miR-155) in these EVs carrying different surface proteins. A 24-microwell chip was fabricated on top of the cover glass to improve analysis throughput, with each well (maximum volume = 10 μl) loaded with one type of the antibody-conjugated NOBs. Liquid mixing in each well was facilitated by spinning the NOBs on a stirrer plate, and a magnet was used to pull down the NOBs during washing and solution exchange. The highly abundant exosomes captured by NOB_{Exo} required only 1 μl of serum for detection, but the NOBs targeting different surface proteins other than the exosomal protein markers needed 5 μl of serum to detect a good number of fluorescent particles. In this step, we only examined a small sample set ($n = 3$ for each cohort of healthy controls or patients with BC) as proof-of-principle study. We found that, for exosomes, the CD44⁺ EVs and the HER2⁺ EVs significantly higher counts of the total stained EVs, i.e., P_{EV} , and the miRNA⁺ EVs, i.e., P_{miRNA} , were detected in patients with BC compared to that in healthy controls, with the CD44⁺ or HER2⁺ EVs showing larger differences than exosomes (fig. S16). The higher number of P_{miRNA} detected in these EVs also could be attributed to the higher loading of miR-21 and miR-122, because their $P_{\text{miRNA}}/P_{\text{EV}}$ ratios were significantly higher in patient sera as well (Fig. 2E and fig. S16). In contrast, the other miRNA marker tested, miR-155, did not exhibit significantly higher $P_{\text{miRNA}}/P_{\text{EV}}$ ratios in patient sera when it was detected in exosomes and the HER2⁺ EVs (Fig. 2E), although its P_{miRNA} increased in these EV subpopulations (fig. S16), supporting that the higher number of the miR-155-bearing exosomes or HER2⁺ EVs found in patients was just due to more EVs secreted. In the meanwhile, most of the results, including P_{EV} , P_{miRNA} , and the ratio of $P_{\text{miRNA}}/P_{\text{EV}}$ for the CD24⁺ EVs, did not show significant differences between patients with BC and healthy controls, except for the $P_{\text{miRNA}}/P_{\text{EV}}$ values for miR-21 and miR-122, which displayed small but statistically significant differences (fig. S16). These results suggest that the abundance of the EVs carrying specific tumor protein like CD44 and HER2 could be enhanced in patients with BC, while the number of exosomes may not show a similarly big difference. In addition, secretion of miR-122 or miR-21 to the exosomes, the CD44⁺ EVs, or the HER2⁺ EVs could be enhanced in patients with BC but not that of miR-155.

Since a larger difference in the $P_{\text{miRNA}}/P_{\text{EV}}$ values between patients with BC and healthy controls was found for miR-122 than for miR-21 within this small sample set and the total number of

exosomes was higher than CD44⁺ or HER2⁺ EVs that permits better detection sensitivity, we expanded our analysis to a relatively larger sample cohort, focusing the miR-122-associated exosomes ($n = 9$ for healthy controls and $n = 8$ for patients with BC). Again, P_{EV} did not show much differences between patients with BC and healthy controls, but both $P_{\text{miR-122}}$ and $P_{\text{miR-122}}/P_{\text{EV}}$ increased in patient samples (fig. S17), and the ratios in patient samples were significantly higher than those in healthy controls ($P < 0.0001$) (Fig. 2F), agreeing with the previous reports on the higher amounts of exosomal miR-122 found in patients with BC and the contribution of miR-122 to BC metastasis (44, 45). These results well justify the necessity of detecting the individual miRNA-associated EVs rather than the bulk EV quantity for recognition of unique EV subpopulations valuable for disease diagnosis.

Assessment of colocalization of tumor proteins and miRNAs in single EV

The results discussed above point out that miRNA loading in EVs carrying different surface markers could vary. Thus, it could be important to detect both protein and miRNA simultaneously on the same EV. This is also rational because the protein cargos are related to EV biogenesis pathways and reflective to the complex physiological states of the cells of origin (21), and the miRNAs could contribute to their roles in cell-cell communication (16). Dual-marker detection can be achieved by labeling each EV captured by the NOB with two fluorescent DNFs (58, 61). Five aptamer-containing ssDNA probes were designed to target the protein markers of CD63, CD44, HER2, EGFR, or MUC1 (fig. S18). Each of these probes was paired with one of the four ssDNA probes containing the complementary sequence of miR-122, miR-21, let-7a, or miR-155 to assess their colocalization with the target proteins (fig. S18). The ssDNA probes also contain the RCA primers that can bind to the target and grow into DNF either labeled by Alexa 647 (for protein detection) or by Alexa 488 (for miRNA analysis). These two RCA systems exhibited very low cross-talk: Mixing the mismatched primer and circular template did not initiate RCA (fig. S18). The specificity of the aptamer-containing probes for protein detection was confirmed by using an antibody to block the target protein on the membrane dyestained EVs captured on the imaging surface by the anti-CD63/CD9/CD81 mixture; for any of the five proteins tested, the proportion of the protein⁺ EVs detected by NOBEL-SPA was markedly reduced (fig. S19).

Figure 3A displays the representative images obtained from dual detection of CD63 and miR-122 on the exosomes isolated by NOB_{Exo} from the purchased EVs. We used CellProfiler (<https://cellprofiler.org/>) for image analysis. This program recognizes the center of the fluorescence intensity of each fluorescent spot to determine the positive hits (i.e., one spot having only one exosome), counts the number of fluorescent spots in each channel, and measures their fluorescence intensities. Using the fluorescence intensity of Alexa 633 (I_{protein}) and Alexa 488 (I_{miRNA}), we can easily tell apart the exosomes carrying only the protein (red arrows in Fig. 3A, $I_{\text{miRNA}} = 0$), only the miRNA (green arrows, $I_{\text{protein}} = 0$), and both markers (yellow arrows). We can clearly see that only a small proportion of the CD63⁺ exosomes were also associated with miR-122. Pairing CD63 with different miRNAs, colocalization analysis of the images gave out low coefficients ranging from 0.132 to 0.481, depending on the identity of the miRNA. The P_{miRNA} counts obtained using the single- (for miRNA) and the dual-marker (for CD63 and miRNA) detection systems exhibited a high Pearson correlation

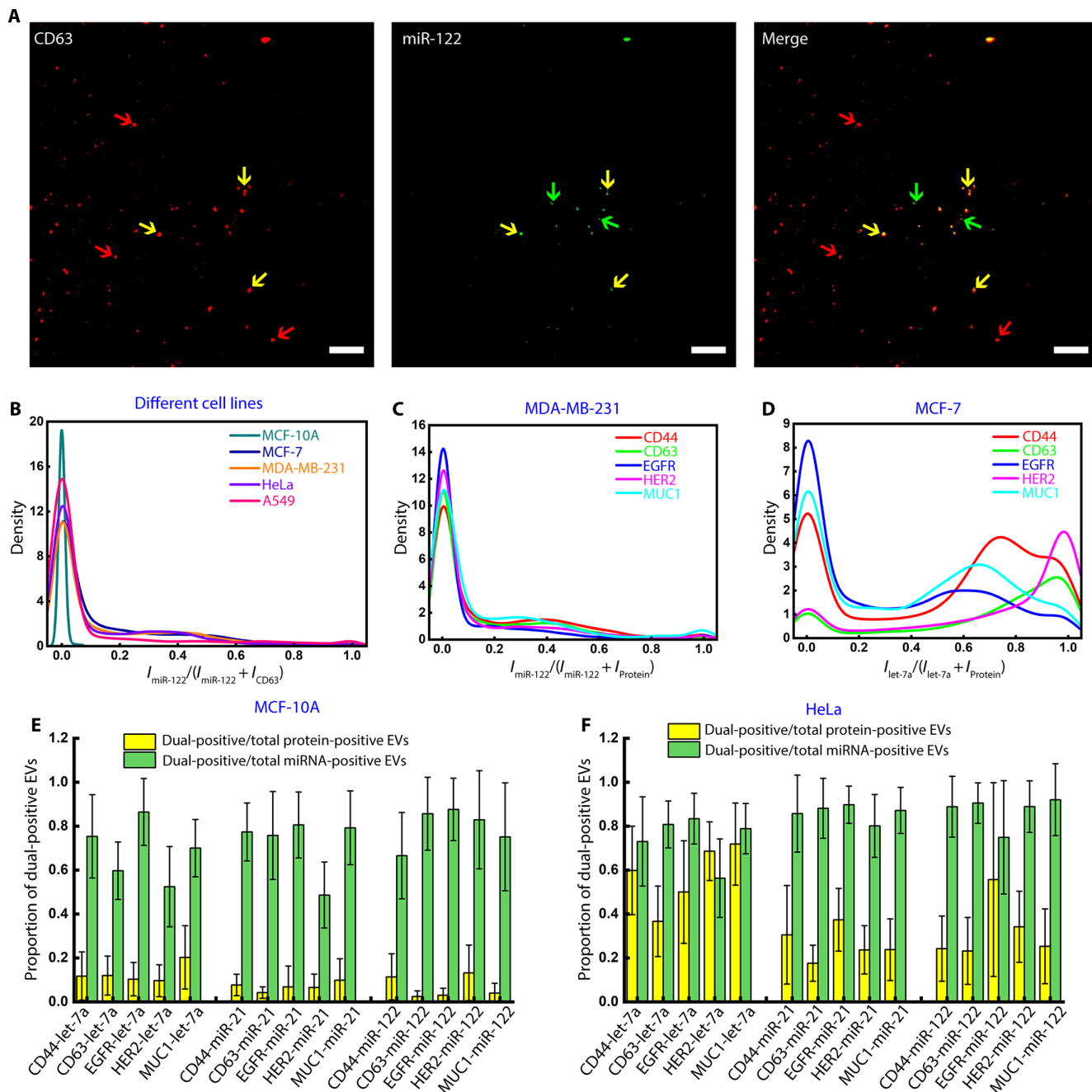


Fig. 3. Dual-marker detection on single EVs. (A) Representative CFM images for dual-marker detection of CD63 and miR-122 by NOBEL-SPA in the exosomes isolated on NOB_{Exo}. Red, green, and yellow arrows point toward the particles emitting signals from only CD63, only miR-122, or both. Scale bars, 10 μm. (B to D) Density distribution profiles of the fluorescence intensity ratios detected for the pair of CD63/miR-122 in five cell lines (B), for miR-122 in the exosomes from MDA-MB-231 (C), and for let-7a in those from MCF-7 with one of the 5 proteins (D). (E and F) Proportion of the dual-positive EVs in the total miRNA⁺ (yellow bars) or protein⁺ (green bars) EVs derived from MCF-10A (E) and HeLa (F) cells. Each reported value and the error bar represent the average and SD of the particle count ratios obtained from 10 images.

coefficient of 0.9777 (fig. S20), proving that dual-marker labeling did not experience noticeable space hindrance and no deviation was found between the miRNA abundance detected by single- and dual-marker.

The above results prove the success of dual-labeling and low interference between the two DNF labels. Then, we applied dual-label NOBEL-SPA to analyze the exosomes harvested from five cell lines,

A549, HeLa, MCF-10A, MCF-7, and MDA-MB-231, using NOB_{Exo} for EV isolation. A total of 20 protein/miRNA combinations were constituted from pairing five proteins and four miRNAs as described above. In each EV sample from the same cell line, 2.4×10^6 EVs were captured by $\sim 10^7$ NOB_{Exo} particles, and 20 images were taken for each protein/miRNA pair. We plotted the density distribution profile of the ratio of $I_{\text{miRNA}}/(I_{\text{protein}} + I_{\text{miRNA}})$ for all the fluorescent

spots detected in 20 images. Spots with a ratio of 0 or 1 were the EVs having only the protein or miRNA signal detected, and those with a ratio close to 0.5 should carry considerable amounts of both protein and miRNA markers. We compared the distribution profiles of the same protein/miRNA pair among the EVs from different cell lines or among the different protein/miRNA pairs from the EVs from the same cell line (figs. S21 to S25). They well reflect the heterogeneous nature of the EVs and the ultralow abundance of those carrying specific markers among all the exosomes captured by the NOBs. Taking the CD63/miR-122 as an example (Fig. 3B), we found that while the CD63⁺/miR-122⁺ subpopulation was barely detected in the exosomes from MCF-10A cells (the curve in cyan blue), they occupied a low proportion in those from A549 cells (the curve in pink) and were found at relatively higher proportions in those collected from MCF-7, MDA-MB-231, and HeLa cells. However, even in these exosomes, miR-122 was only found in a very small proportion of the population. Comparing the distribution profiles of the exosomes marked by miR-122 and various protein markers, we found slightly higher population densities for the MDA-MB-231 exosomes carrying both miR-122 and the protein marker of CD63, CD44, or MUC1 (i.e., the intensity ratios in the range of 0.4 to 0.6), compared to HER2 and EGFR (Fig. 3C). In contrast, another miRNA, let-7a, was detected in a large proportion of the MCF-7 exosomes carrying CD44, EGFR or MUC1 but not in those with HER2 or CD63 (Fig. 3D). Similar to our results from single marker detection in exosomes captured by various surface proteins displayed in Fig. 2E, miR-155 was much more abundant than other miRNAs in all samples: Not only there was a substantial proportion of the exosomes emitting the signal from miR-155, most of them also detected simultaneously with the marker proteins (figs. S21 to S25).

To assess the situation of protein/miRNA colocalization in more details, we evaluated the proportion of the miRNA⁺ exosomes among the total protein⁺ exosomes and vice versa (fig. S26). We notice that, for let-7a, miR-21, and miR-122, the proportion of the protein⁺/miRNA⁺ exosomes among the miRNA⁺ ones, i.e., including both the protein⁺/miRNA⁺ and protein⁻/miRNA⁺ subpopulations, was >70% in most cases, much higher than their proportion among the protein⁺ subpopulations, including both the protein⁺/miRNA⁺ and protein⁺/miRNA⁻ subgroups (Fig. 3, E and F, and fig. S26). In the MCF-10A-derived exosomes, there was only <10% of the protein⁺ exosomes encapsulating the miRNA, further proving the low abundance of tumor miRNAs in the exosomes secreted by the nontumorigenic cells (Fig. 3E). Our results support that the presence of protein markers in exosomes is more ubiquitous than these specific tumor miRNAs. Still, some exceptions exist. For example, the proportion of the dual-positive exosomes among the let-7a⁺ exosomes increased to >40% in those from MCF-7 and HeLa cells. Close to 70% of the let-7a⁺ exosomes derived from HeLa cells associated with HER2 or MUC1 (Fig. 3F), suggesting the high possibility of colocalization of let-7a with these tumor proteins in such exosomes. In addition, similar to the situation found in the test of the small set of clinical samples shown in Fig. 2E, miR-155 was present abundantly in the exosomes from all cell lines, colocalized with all of the proteins tested, particularly in the exosomes from MCF-7 and HeLa cells.

EVs with dual markers in BC diagnosis

We hypothesize that the exosomes carrying both the tumor protein and miRNA could have high potential in differentiating patients

with cancer from healthy controls. To test this, we segregated the exosomes into three categories: protein-only [$I_{\text{miRNA}}/(I_{\text{protein}} + I_{\text{miRNA}}) = 0$], miRNA-only [$I_{\text{miRNA}}/(I_{\text{protein}} + I_{\text{miRNA}}) = 1$], or dual-marker [$0 < I_{\text{miRNA}}/(I_{\text{protein}} + I_{\text{miRNA}}) < 1$]; counted the numbers of exosomes in each category; and calculated the proportion of each category among the total detected exosomes. Figure 4A is the heatmap of the average (from 20 images) proportions of the dual-marker category detected in the EVs derived from five cell lines (five columns), testing 20 protein/miRNA combinations (20 rows). Subjecting the proportions of the dual-marker category detected for all of the protein/miRNA pairs (20 variables) in all images (20 repeats for each cell line) to canonical discriminant analysis (CDA), excellent classification of the exosomes by their cells of origin was achieved (Fig. 4B), with an error rate of 1% (fig. S27). The separation effect was worse if the proportions of the protein-only (Fig. 4C and figs. S28 and S29) or miRNA-only (figs. S28 and S30) category were subject to CDA.

To reveal the most important protein/miRNA pairs for the differentiation effect, we analyzed the dataset with the machine learning algorithm of support vector machine-recursive feature elimination (SVM-RFE), as done in our other published works (69, 70). To find the protein/miRNA combinations suitable for BC diagnosis, we separated the five cell lines into four classes, non-BC tumors (A549 and HeLa), MCF-10A (nontumor), MCF-7 (nonmetastasis BC), and MDA-MB-231 (metastasis BC). Five protein/miRNA pairs, CD44/miR-21, CD44/miR-155, CD63/miR-122, HER2/let-7a, and MUC1/let-7a, all belonging to the dual-marker category, were found to be the most important features for cell line differentiation. These five features are sufficient to classify the cell lines with satisfactory accuracy (0.800), specificity (0.927), sensitivity (0.800), and the area under the curve (AUC) (0.957), when tested by 10-fold cross-validation.

To further assess the diagnostic power of the five protein/miRNA combinations found above in clinical samples, we used NOBEL-SPA to examine human sera taken from healthy controls ($n = 18$), and stage I ($n = 11$), and stage II ($n = 9$) BC patients with matching ages. For each protein/miRNA pair, only 1 μl of human serum was used to mix with 10 μg of NOB_{Exo} for exosome capture. Like in the cell line analysis, each CFM image was considered as one repeated measurement of the clinical sample, and each protein/miRNA pair considered as one variable in statistical analysis. From the violin plots of the proportion of each category: protein-only, miRNA-only, or dual-marker (Fig. 5 and figs. S31 and S32), we found the proportions of both the CD63⁺/miR-122⁺ and CD44⁺/miR-21⁺ exosomes (enclosed in the two red rectangles in the dual-marker plot in Fig. 5A) increased significantly in patients with BC compared to healthy controls. In the protein-only category, the CD44⁺/miR-155⁻ or HER2⁺/let-7a⁻ exosomes showed large and statistically significant increase ($P < 0.0001$) in stage I patients compared to healthy controls (fig. S31). The good marker potential of CD44 and HER2 has also been revealed in our previous work (58). On the other hand, in the miRNA-only category, the HER2⁻/let-7a⁺ showed significant decrease ($P < 0.0001$) in stage I patients compared to healthy controls, which is in the opposite trend as that occurred to the HER2⁺/let-7a⁻ exosomes. Such a phenomenon was also seen for the pair of CD44/miR-155 (enclosed in the blue rectangles in the protein-only and miRNA-only plot in Fig. 5A). Similarly, we observed the negative correlation in the cell line-derived exosomes as well: The density distribution profiles showed high density of the let-7a-only

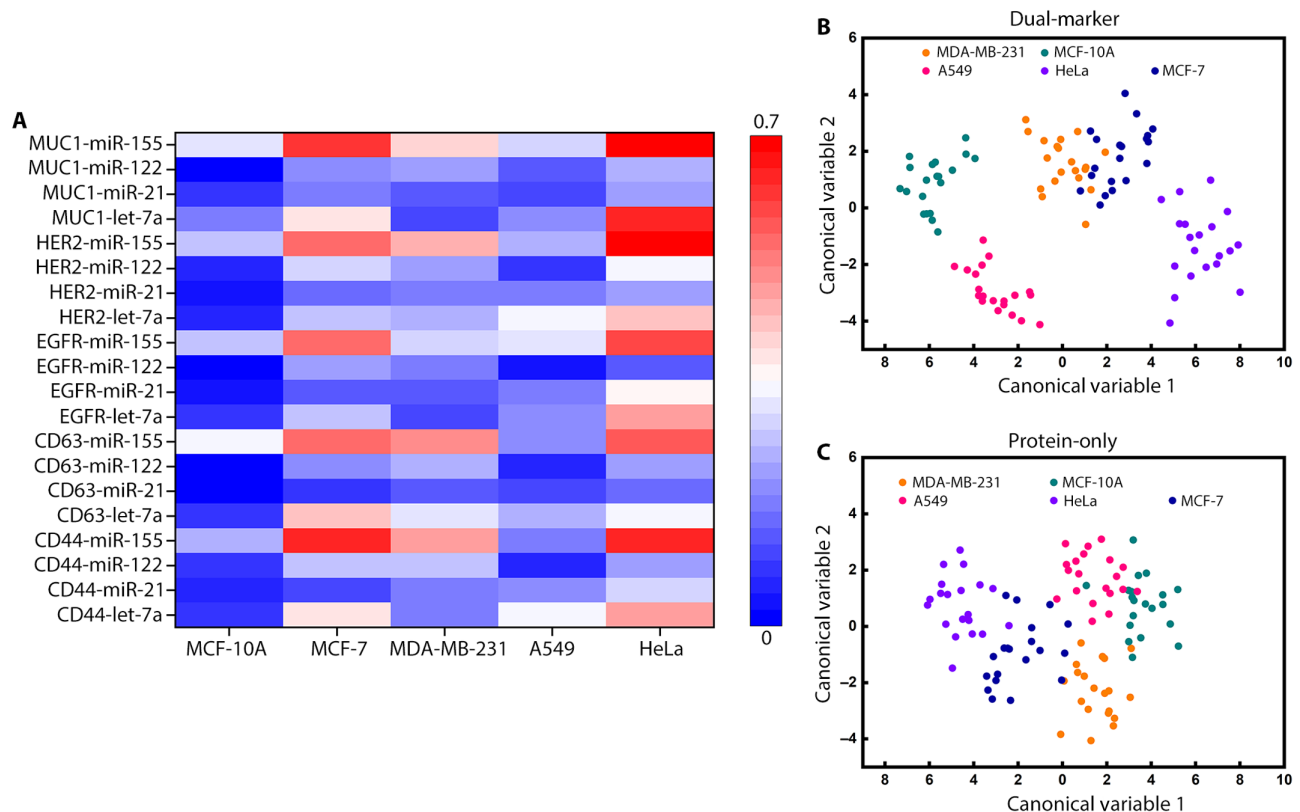


Fig. 4. Differentiation of EVs by cells of origin based on the profiles of protein/miRNA combination. (A) Heatmap of the proportions of the protein⁺/miRNA⁺ exosomes by among the total population detected in the EVs from different cells lines. (B and C) Canonical score plots using the proportions of the dual-marker exosomes (B) or those with only proteins (C) showing different degrees of classification of the exosomes based on the cells of origin. NOB_{Exo} was used for EV capture.

exosomes accompanied with the much reduced density of the HER2-only ones in those derived from HeLa and MCF-7 cells (figs. S22 and S23), but the trend was reversed for those obtained from MDA-MB-231 cells (fig. S24).

Because SVM-RFE using the data collected from BC-related cell lines revealed the five protein/miRNA pairs as potential markers to classify the nontumor, non-BC, nonmetastasis BC, and metastasis BC cells, we examined their potential in BC diagnosis by subjecting their population proportions observed in all images collected from the clinical samples for *t*-distributed Stochastic Neighbor Embedding (*t*-SNE). The resultant scatterplot clearly separates patients with BC from the health controls, with the data points from each cohort nicely clustered together (Fig. 5B). Unfortunately, *t*-SNE did not show clusters of the two different BC stages, but one of the five combinations, the CD63⁺/miR-122⁺ exosome subpopulation, exhibited continuous and significant increase between healthy controls, stage I, and stage II BC patients (Fig. 5C). Such a gradual change was not observed for other subpopulations.

While *t*-SNE is an unsupervised nonlinear dimensionality reduction technique aiming to visualize the relationships embedded among the data, we expect that machine learning approaches could help confirm the possibility of building prediction models using the colocalization information of the selected protein/miRNA pairs for early BC diagnosis. Although the dual-marker pairs can differentiate the cell lines by their tumorigenicity and metastatic potential, clinical samples are more complicated than cell lines, requiring more

variables to establish the prediction model. Thus, we attempted the SVM-RFE algorithm on the dataset containing the proportions of both the dual-marker and the protein-only exosomes found in the clinical samples, hoping to obtain a classification model that permits the use of the proportions of these two exosome subpopulations from an “unknown” sample to predict its disease class. Two goals were tested. The one was to classify healthy controls and patients with BC, and the other was to differentiate healthy controls, stage I BC, and stage II BC. The classification model was then tested by five repeats 10-fold cross-validation to assess its performance, using metrics like accuracy, sensitivity, specificity, precision, and AUC. Agreeing with the *t*-SNE results, differentiation of patients with BC from healthy controls is successful, with all metrics close to 1 (table S2). The classification performance obtained by using the dual-marker and the protein-only or miRNA-only combinations was comparable (table S2). BC stage classification is more difficult, but still, scores for accuracy, specificity, and precision were ~0.8 and for sensitivity and AUC were larger than 0.9 (table S3). If only the dual-marker subpopulation was used for classification, then excellent performance metric scores still are achieved for differentiation of patients from healthy controls (table S4), while the values decreased slightly from those acquired using two subpopulations (table S5). Power analysis found that a sample size of 38 would be needed to reach a classification accuracy value of 0.80 with $\alpha = 0.05$ for differentiation of healthy versus patients with BC, but a larger size of 86 was found for differentiation of healthy controls and stage I or II BC patients.

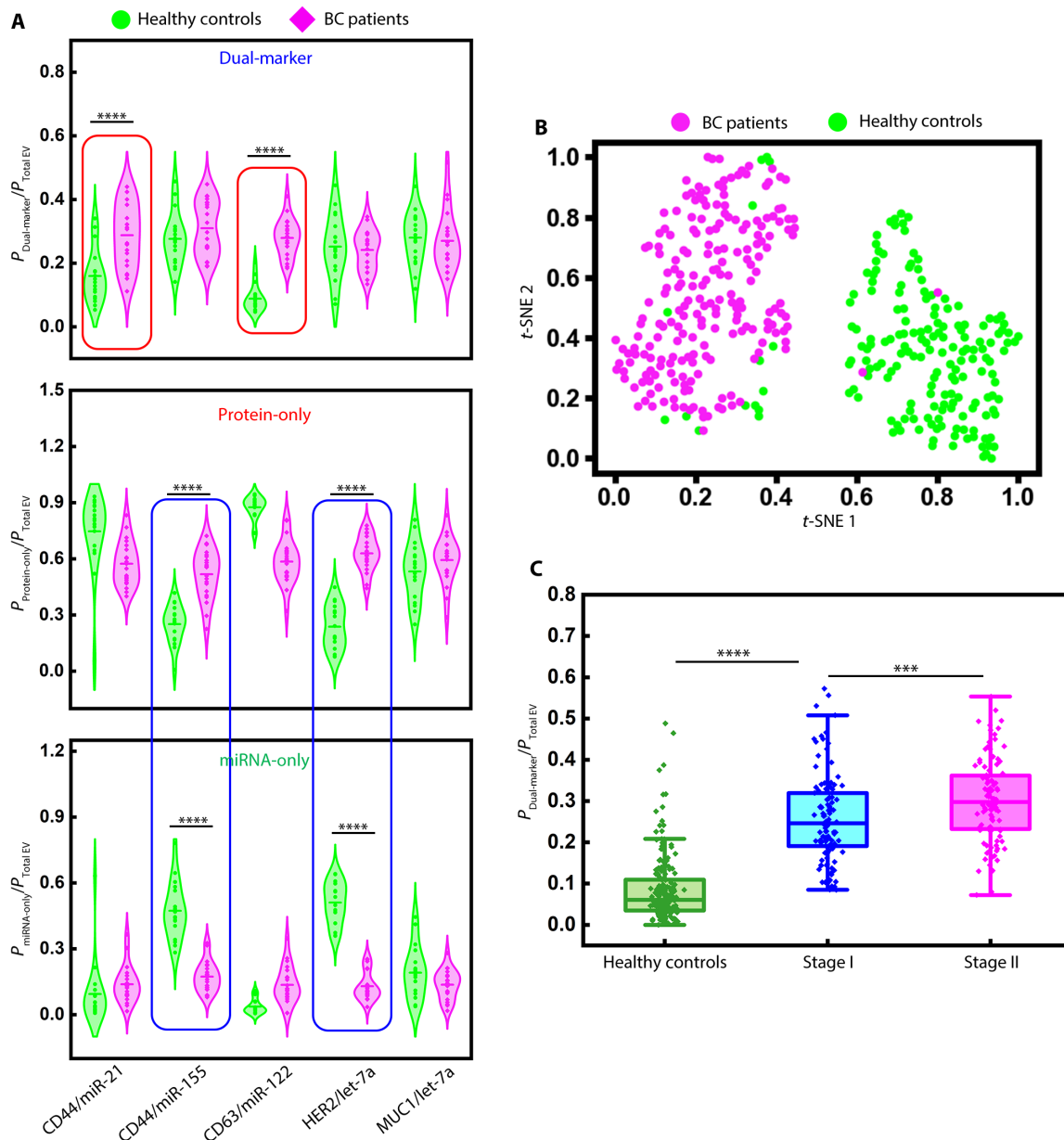


Fig. 5. EV subpopulations for BC diagnosis. (A) Violin plots of the proportions of the different exosome subpopulations (protein⁺/miRNA⁺, protein⁺/miRNA⁻, and protein⁻/miRNA⁺) among the total exosomes detected by using NOB_{Exo} in sera samples collected from healthy controls and patients with BC. (B) t-SNE scatterplot showing successful differentiation of patients with BC from healthy controls using the population proportions of the exosomes carrying the dual-marker pairs of CD44/miR-21, CD44/miR-155, CD63/miR-122, HER2/let-7a, and MUC1/let-7a. Green dots represent healthy controls, and the pink dots represent patients with BC. (C) Box plots of the proportions of the CD63⁺/miR-122⁺ exosome subpopulations among the total exosomes detected in sera samples collected from healthy controls ($n = 18$) and stage I ($n = 11$) or II ($n = 9$) BC patients. A total of 10 images were taken for each clinical sample. *** $P < 0.001$; **** $P < 0.0001$.

DISCUSSION

EVs carry high potential as the biomarkers in liquid biopsy, because they are easily accessible in all body fluids, their biogenesis involves distinct intracellular processes regulated by the physiological states of the parental cells, and they enclose many cargo molecules including proteins and nucleic acids that can serve the purpose of cell-cell communications. While they have so many attractive features, it is very challenging to identify the disease-relevant EV subpopulations among the swarm of highly heterogeneous EVs produced by all

cells. Although the conventional or advanced separation techniques can sort the EVs by properties like size, shape, density, surface hydrophobicity, etc., even the very thorough separation procedure could recover heterogeneous EVs (71). Bulk analysis only produces the ensemble average of the varying signals from a swarm of heterogeneous EVs, missing the signals from the distinct subgroups at trace levels that carry out specific disease-related functions or are derived from cells undergoing pathological transition (21, 25). It has been well demonstrated by the pioneering developments that

detecting cargos on single EVs can overcome the heterogeneity issue and unambiguously identify the few EVs bearing unique phenotypic features, such as a panel of protein markers or a selection of miRNAs, among the overwhelming disease-irrelevant populations. Hence, the goal of our work is to establish a broadly adaptable platform that can simplify single EV analysis and rapidly detect multiple types of EV cargos on individual EVs for improved specificity.

NOBEL-SPA achieves this goal by using the easily manipulated magnetic NOBs that can rapidly and efficiently isolate EVs from a small volume of biofluids. The fast and highly efficient EVs capture by the NOBs are the results of their spinning feature while placed in a rotation magnetic field, which can speed up molecular transfer to the sensor surface and improve the binding kinetics. Fast molecular transfer also can help remove loosely bound impurities. In addition, the easiness in handling the NOBs by a magnet simplifies the entire assay. They can be rapidly removed from the solution because of their superior superparamagnetic property and redistributed with good dispersity owing to the high surface charges. All these features ensure a fast turnaround time of our method and complete EV isolation, labeling, and imaging in 4 hours. EVs with concentrations as low as few or tens EV particles/ μl are detectable (Fig. 1). The comparable dimension of each NOB to the EVs with diameters ~ 100 nm permit the capture of only one to two EVs per NOB to effectively eliminate EV aggregation (Fig. 1). To further reduce the possibility of loading more than one EV on each NOB, we used a mole ratio between NOBs and antibody of 10:1 during antibody conjugation and used a large number (10^6) of the NOBs to capture the EVs from biological samples. For example, 10^6 NOBs were used to capture exosomes from 1 μl of serum in the present work, which may contain only $<10^5$ exosomes. Our method of avoiding EV aggregation in single EV analysis could be more easily implemented than controlling the EV input by sample dilutions or specifically locating single EVs on the sophisticated designed sensor surface. Moreover, once the EVs are lysed to expose the intravesicular components, they can be immobilized on each NOB to maintain their high, local concentrations, permitting the detection of miRNAs in individual EVs the abundance of which could be as low as one copy per thousand EV particles when quantified by the conventional method of RT-PCR.

About one in eight US women will develop invasive BC over the course of her lifetime, and BC has a higher death rate than most common cancers except lung cancer (breastcancer.org). Since $\sim 85\%$ of the BC cases occur in patients with no family history, frequent, noninvasive examination is the most useful manner for capturing the onset of the disease at an early stage to improve cure and reduce mortality. However, BC is highly heterogeneous and encompasses distinct subtypes exhibiting diverse clinical features (72–74). Biomarkers that can handle high disease heterogeneity and clearly differentiate BC stages and subtypes are thus highly valuable for BC diagnosis, prognosis, and therapeutic monitoring (6, 75). EVs derived from tumor cells could be ideal for such purposes because they carry a collection of molecules either inherited from the parent tumor cells, like surface proteins (8, 22, 32, 35, 37, 55) or selectively packaged, like miRNAs, for physiological regulation (41, 53), affecting tumor growth, tissue invasion, and metastasis (44, 45). The present work focused on two types of tumor markers: proteins and miRNAs enclosed in single EVs. The tumor proteins could reveal the EV's tumor origin, and the miRNAs may indicate the EV's potential in affecting the cellular processes like cell proliferation

(76), inflammation responses (77), or metabolism (44, 45) in the recipient cells. NOBEL-SPA can easily recognize individual EVs carrying both the protein and miRNA markers, since its signal amplification approach is based on long DNA chains, i.e., DNFs, grown on the primer attached to the target recognition probes, which could be either antibodies, aptamers, or target-complementary ssDNAs. By simply switching the target recognition probes, detection of diverse EV cargos like mRNAs, DNAs, lipids, etc. can be done. Moreover, as described above, the design of NOB can ensure that, at most, only one EV can be captured by each NOB, and CellProfiler can automatically distinguish the aggregated and clumped EVs and recognizes objects that exhibit a single peak of fluorescence, e.g., showing higher intensity toward the interiors but dimmer toward the edges. These fine controls, along with the threshold application in CellProfiler to exclude any dots larger than 20 pixels, and the usage of its MaskObject function to find the individual objects identified in each fluorescence channel that are overlapped at the same position can help determine individual EVs carrying both protein and miRNA or only having the protein or miRNA but not both.

By using NOBEL-SPA to detect the subpopulations of EVs carrying unique signatures, we find that, while the total exosome number did not show any significant difference between the patients with BC and the healthy controls, the proportion of the miR-122⁺ exosomes displayed much larger and statistically significant differences (Fig. 2). Further refining the miR-122⁺ exosomes to be the CD63⁺/miR-122⁺ subpopulation can even help differentiate stage I and stage II BC patients, while both patient categories were well distinct from the healthy controls (Fig. 5). Moreover, compared to detecting only the proteins or only the miRNAs, simultaneous detection of proteins and miRNAs can perform better in differentiating the tumor cell lines, indicating the necessity of targeting multiple types of cargos on single EVs if higher specificity in diagnosis and prognosis is to be obtained.

Besides enhancing diagnosis specificity, recognizing multiple cargo molecules on single EVs can improve our understanding of EV cargo loading. The present work focused on exosomes by capturing the EVs using the antibodies against CD63/CD9/CD81. One interesting phenomenon we noticed from our results is that the selected protein markers are more ubiquitously found in exosomes, but only a very small proportion of them carried the marker miRNAs (fig. S26). On the other hand, rarely the miRNA marker would be detected by itself in the tumor-derived exosomes without the presence of any of the protein markers. These results well agree with the previous research findings about the selective sorting of the signaling miRNAs to EVs, which could carry out the function of cell-cell communication during tumor development and metastasis (44, 45, 53). For the ones selectively sorted to exosomes, like miR-122, detecting it along with the colocalized protein, like CD63, could then help with early BC diagnosis. For the proteins and miRNAs having opposite roles in promoting the growth of cancer cells, like let-7a and HER2 (76, 78), colocalization analysis also revealed their negative correlation in the exosomes derived from certain cells (fig. S22 to S24) and in human sera (Fig. 5A), indicating that their loading into EVs could follow different mechanisms and could be related to the functions of these markers. It has been reported that HER2 can promote the growth of cancer cells, but let-7a can suppress migration and invasion of BC cells (76, 78). Future studies following the single EV analysis can compare the abundances of different cargo molecules in the parental cells to gain deeper understanding of the cargo loading mechanisms.

The amplification strategy used by NOBEL-SPA permits biomarker detection of <100 vesicles in 1 μ l of serum in the present work. The low sample consumption and high sensitivity, accompanied with the easy handling of the magnetic NOBs, make NOBEL-SPA suitable for analysis of large number of samples. Then, the premise of the EV subpopulations simultaneously carrying the dual-marker protein/miRNA pairs as disease markers can be further validated by NOBEL-SPA in the large-scale test of clinical samples. Classification models established using the SVM algorithm prove the potential of using both the dual-marker and protein-only or miRNA-only groups to successfully assign the clinical samples between the healthy and BC category (table S2). Our BC samples include stage I BC patients, highlighting the power of our technique in early cancer diagnosis which is very critical for timely treatment and survival rate improvement. The classification performance of using only the dual-marker subpopulation was comparable to using two subpopulations for prediction of healthy people and BC patients (table S4), supporting the importance of finding the exosomes carrying both tumor proteins and tumor marker miRNAs in diagnosis. To identify such subpopulations, single vesicle analysis is necessary and carries superior power over bulk analysis in marker discovery.

Differentiating between stages I and II is more challenging (table S3) but still achievable by analyzing the colocalization of one or few pairs of protein and miRNA markers on single EVs as demonstrated in Fig. 5C for the exosomes carrying both CD63 and miR-122. While CFM could be somewhat technically demanding, these specific EV subpopulations discovered by NOBEL-SPA can be targeted in bulk analysis like ELISA or lateral flow devices that are more suitable for point-of-care clinical testing owing to easy and low-cost operation. For example, the EVs can be enriched via recognition of the surface protein marker, and the enclosed miRNA can be detected to achieve high sensitivity and specificity in clinical diagnosis and prognosis.

Besides EVs, NOBEL-SPA should have broad applicability for other targets. This technique should also have broad applicability for analysis of other biological vesicles with submicron sizes at the single particle level. For example, NOBEL-SPA can be applied to detect viruses in clinical samples, which are also as small as EVs and highly heterogeneous, present at low abundances at the early stage of infection. Capturing the small population of the viral particles carrying the mutated nucleic acid sequences and the highly infectious surface proteins is highly important for timely control of the pathogen spread.

In summary, the present work has achieved both knowledge and technical advancements. The former is represented by the discovery of the value of EV subpopulations defined by the colocalization of certain protein/miRNA pairs in diagnosis of early-stage cancer. The latter is the successful development of the enabling technique of NOBEL-SPA that can carry out single EV analysis in a highly sensitive and effective manner and can assess the colocalization of protein and nucleic acid markers in the same EV, tasks not yet been accomplished by current techniques with matching assay efficiency and sensitivity (table S1). While the technique of NOBEL-SPA can have broad applicability in analysis of other submicron biological particles, the colocalization assessment can help study the loading mechanisms of nucleic acids to EVs during disease development, leading to new therapeutic approaches by studying their production and functions. Although the diffraction-limited confocal fluorescence microscopy

may not be readily used in clinical laboratories, we envision that NOBEL-SPA will be valuable in advancing EV marker discovery. The identified EV markers can then be used in the development of bulk analysis methods suitable for rapid clinical testing.

MATERIALS AND METHODS

Preparation of bioconjugated NOBs

The magnetic Fe₃O₄@SiO₂ nanorods were synthesized according to the reported protocol (62). Then, they were incubated with the carboxyl-modified (3-aminopropyl) triethoxysilane in dimethylformamide at room temperature for 36 hours, ready for antibody conjugation via EDC/NHS coupling. The remaining activated carboxyl groups on the surface were deactivated by glycine. The obtained NOBs were redispersed in 1 \times phosphate-buffered saline (PBS) at a concentration of 1 mg/ml and stored at 4°C. NOBs conjugated with the mixture of antibodies against the exosomal markers of CD63, CD81, and CD9, i.e., NOB_{Exo}, were used, except for the data presented in Fig. 2E, the collection of which also used the NOBs coupled with the antibody against HER2 (NOB_{HER2}), CD44 (NOB_{CD44}), or CD24 (NOB_{CD24}). More details can be found in the Supplementary Materials.

NOBEL-SPA

The wells for the assay were firstly blocked by 0.1% bovine serum albumin (BSA) in 1 \times PBS overnight to reduce nonspecific adsorption. Ten microliters of NOBs (10 ng/ml) was added to each well and mixed with 10 μ l of the EV sample. The chip was placed on the stirring plate set at 360 rpm. After 30-min EV capture, the NOBs were pulled down by a magnet and washed with 1 \times PBS and then sequentially mixed with 4% PFA and 0.1 M EDC in 0.1 M imidazole buffer (pH 8) to fix the captured EV and crosslink the nucleic acid. The residual reagents were washed away with 0.2% glycine. Followed, a mixture of 1 μ l of 10 \times phi29 buffer [500 mM tris-HCl, 100 mM MgCl₂, 100 mM (NH₄)₂SO₄, and 40 mM dithiothreitol], 1 μ l of BSA (0.125 mg/ml), 1 μ l of 0.05 μ M circular probe, 1 μ l of 0.25 μ M recognition probe, 1 μ l of 0.5 \times DiB, and 6 μ l of deionized water was added and incubated for 30 min at room temperature on the magnetic stir plate (360 rpm) to recognize the target miRNA and stain the captured EVs. After that, 1 μ l of 200 μ M deoxynucleotide triphosphate (dNTP), 1 μ l of 2.5 μ M biotin-deoxyadenosine triphosphate, and 1 μ l of phi29 DNA polymerase (2.5 U/ml) were added to the well and incubated at 37°C for 30 min. Last, 1 μ l of 2.5 μ M streptavidin-modified Alexa 633 was added, and the solution was incubated for 30 min. After washed with 1 \times PBS three times and dispersed in 10 μ l of 1 \times PBS, the NOBs were ready for CFM.

Dual-marker NOBEL-SPA followed a similar procedure with some modifications: (i) RCA used a mixture of two circular probes, 1 μ l of each at 0.05 μ M, and target recognition probes for the protein and miRNA markers, 1 μ l of each at 0.25 μ M; (ii) the RCA reaction buffer contained 1 μ l of 1 mM dNTP; and (iii) after RCA, a mixture of detection probes (Alexa 488 for miRNA and Alexa 647 for surface protein) was added, each supplied at 1 μ l of 2.5 μ M and incubated for 30 min.

In the RNase treatment tests, the EVs captured by the NOBs were treated by 40 U of RNase If in 11- μ l NEBuffer 3 at 30°C for 20 min (44). After washing the RNase-treated EVs with 1 \times PBS for three times, general NOBEL-SPA for miRNA detection was carried out.

Confocal microscopy and image analysis

Fluorescence imaging was performed on a Zeiss 880 Inverted Confocal Microscope using an ultraviolet laser with $\lambda_{\text{ex}} = 330$ nm, an Argon laser with $\lambda_{\text{ex}} = 488$ nm, and a HeNe laser at $\lambda_{\text{ex}} = 633$ nm for fluorescence from DiB, Alexa 488, and Alexa 633 (or Alexa 647), respectively. All CFM images were collected at a resolution of 512×512 pixels. The viewing area was $100 \mu\text{m}$ by $100 \mu\text{m}$. For each sample, 10 images were acquired at 10 different locations from a single well. The raw data obtained from CFM were exported to the tiff format via ZEN 3.2 (blue edition). The images were processed by CellProfiler with a lab-built pipeline. In this pipeline, the clumped cluster was divided by the intensity, and the size smaller than 20 pixels was regarded as one spot. The number of particles, the size, and fluorescence intensity detected on each particle were automatically collected by the pipeline. More details can be found in the Supplementary Materials.

Statistical analysis

Data plots, statistical analysis, and CDA were carried out by Origin 2021. Differences with $P < 0.05$ were considered as statistically significant. The t -SNE was performed to reduce the dimensionality of complex data by Python 3.9 (64-bit) with the following parameters: `n_components = 2`, `init = "pca"`, `verbose = 1`, `random_state = 123`, `perplexity = 15`, `learning_rate = "auto"`, `n_iter = 5000`. The two-dimensional data were plotted by the `matplotlib.pyplot`. Feature selection and classification were performed with Python 3.9 (64-bit), using `StandardScaler` for data standardization, `SVM-RFE` to select the top five sensors according to weight vectors by the iteration process of the backward removal of features, and `RFE [estimator = svm.SVC (kernel = "linear"), n_features_to_select = 5]`. Performance metrics for the classification evaluation were calculated by using `RepeatedStratifiedKfold (n_splits = 10, n_repeats = 3)` for cross-validation and with `svm.SVC (kernel = "linear")` as the estimator. For the power analysis, `analysis.solve_power (effect_size = effect_size, power = 0.8, alpha = 0.05)` was used, and the `effect_size` was calculated based on the observed accuracy and baseline accuracy (1/3). For the k -fold cross-validation with SVM as the model, `SVC (probability = True, decision_function_shape = "ovr", class_weight = "balanced", cache_size = 2000)` and `RepeatedStratifiedKfold (n_splits = 10, n_repeats = 5, random_state = 123)` were used.

Supplementary Materials

This PDF file includes:

Supplementary Text
Figs. S1 to S32
Tables S1 to S5
Legends for data S1 and S2

Other Supplementary Material for this manuscript includes the following:

Data S1 and S2

REFERENCES AND NOTES

- N. Iraci, T. Leonardi, F. Gessler, B. Vega, S. Pluchino, Focus on extracellular vesicles: Physiological role and signalling properties of extracellular membrane vesicles. *Int. J. Mol. Sci.* **17**, 171 (2016).
- E.-M. Kraemer-Albers, A. F. Hill, Extracellular vesicles: Interneural shuttles of complex messages. *Curr. Opin. Neurobiol.* **39**, 101–107 (2016).
- D. A. Shifrin Jr., M. D. Beckler, R. J. Coffey, M. J. Tyska, Extracellular vesicles: Communication, coercion, and conditioning. *Mol. Biol. Cell* **24**, 1253–1259 (2013).
- G. Turturici, R. Tinnirello, G. Sconzo, F. Geraci, Extracellular membrane vesicles as a mechanism of cell-to-cell communication: Advantages and disadvantages. *Am. J. Physiol.* **306**, C621–C633 (2014).
- M. Yanez-Mo, P. R. M. Siljander, Z. Andreu, A. B. Zavec, F. E. Borrás, E. I. Buzas, K. Buzas, E. Casal, F. Cappello, J. Carvalho, E. Colas, A. Cordeiro-da Silva, S. Fais, J. M. Falcon-Perez, I. M. Ghorbali, B. Giesel, M. Gimona, M. Graner, I. Gursel, M. Gursel, N. H. H. Heegaard, A. Hendrix, P. Kierulff, K. Kokubun, M. Kosanovic, V. Kralj-Iglic, E.-M. Kramer-Albers, S. Laitinen, C. Lasser, T. Lener, E. Ligeti, A. Line, G. Lipps, A. Llorente, J. Lotvall, M. Mancek-Kerber, A. Marcilla, M. Mittelbrunn, I. Nazarenko, E. N. M. Nolte-'t Hoen, T. A. Nyman, L. O'Driscoll, M. Olivan, C. Oliveira, E. Pallinger, H. A. Del Portillo, J. Reventos, M. Rigau, E. Rohde, M. Sammar, F. Sanchez-Madrid, N. Santarem, K. Schallmoser, M. S. Ostendorf, W. Stoorvogel, R. Stukelj, S. G. Van der Grein, M. H. Vasconcelos, M. H. M. Wauben, et al., Biological properties of extracellular vesicles and their physiological functions. *J. Extracell. Vesicles* **4**, 27066–27066 (2015).
- E. Crowley, F. Di Nicolantonio, F. Loupakis, A. Bardelli, Liquid biopsy: Monitoring cancer-genetics in the blood. *Nat. Rev. Clin. Oncol.* **10**, 472–484 (2013).
- A. L. Cicero, P. D. Stahl, G. Raposo, Extracellular vesicles shuffling intercellular messages: For good or for bad. *Curr. Opin. Cell Biol.* **35**, 69–77 (2015).
- A. Hoshino, H. S. Kim, L. Bojmar, K. E. Gyan, M. Cioffi, J. Hernandez, C. P. Zambirinis, G. Rodrigues, H. Molina, S. Heissel, M. T. Mark, L. Steiner, A. Benito-Martin, S. Lucotti, A. Di Giannatale, K. Offer, M. Nakajima, C. Williams, L. Nogués, F. A. P. Vatter, A. Hashimoto, A. E. Davies, D. Freitas, C. M. Kenific, Y. Ararso, W. Buehring, P. Lauritzen, Y. Ogitani, K. Sugiyama, N. Takahashi, M. Alečković, K. A. Bailey, J. S. Jolliss, H. Wang, A. Harris, L. M. Schaeffer, G. Garcia-Santos, Z. Posner, V. P. Balachandran, Y. Khakoo, G. P. Raju, A. Scherz, I. Sagi, R. Scherz-Shouval, Y. Yarden, M. Oren, M. Malladi, M. Petriccione, K. C. De Braganca, M. Donzelli, C. Fischer, S. Vitolano, G. P. Wright, L. Ganshaw, M. Marrano, A. Ahmed, J. DeStefano, E. Danzer, M. H. A. Roehrl, N. J. Lacayo, T. C. Vincent, M. R. Weiser, M. S. Brady, P. A. Meyers, L. H. Wexler, S. R. Ambati, A. J. Chou, E. K. Slotkin, S. Modak, S. S. Roberts, E. M. Basu, D. Diolaiti, B. A. Krantz, F. Cardoso, A. L. Simpson, M. Berger, C. M. Rudin, D. M. Simeone, M. Jain, C. M. Ghajar, S. K. Batra, B. Z. Stanger, J. Bui, K. A. Brown, V. K. Rajasekhar, J. H. Healey, M. de Sousa, K. Kramer, S. Sheth, J. Baisch, V. Pascual, T. E. Heaton, M. P. La Quaglia, D. J. Pisapia, R. Schwartz, H. Zhang, Y. Liu, A. Shukla, L. Blavier, Y. A. DeClerck, M. LaBarge, M. J. Bissell, T. C. Caffrey, P. M. Grandgenett, M. A. Hollingsworth, J. Bromberg, B. Costa-Silva, H. Peinado, Y. Kang, B. A. Garcia, E. M. O'Reilly, D. Kelsen, T. M. Trippett, D. R. Jones, I. R. Matei, W. R. Jarnagin, D. Lyden, Extracellular vesicle and particle biomarkers define multiple human cancers. *Cell* **182**, 1044–1061.e1018 (2020).
- E. Cocucci, J. Meldolesi, Ectosomes. *Curr. Biol.* **21**, R940–R941 (2011).
- E. Cocucci, G. Racchetti, J. Meldolesi, Shedding microvesicles: Artefacts no more. *Trends Cell Biol.* **19**, 43–51 (2009).
- P. I. Hanson, A. Cashikar, Multivesicular body morphogenesis. *Annu. Rev. Cell Dev. Biol.* **28**, 337–362 (2012).
- P. J. Quesenberry, L. R. Goldberg, J. M. Aliotta, M. S. Dooner, M. G. Pereira, S. Wen, G. Camussi, Cellular phenotype and extracellular vesicles: Basic and clinical considerations. *Stem Cells Dev.* **23**, 1429–1436 (2014).
- G. Raposo, W. Stoorvogel, Extracellular vesicles: Exosomes, microvesicles, and friends. *J. Cell Biol.* **200**, 373–383 (2013).
- D. Teis, S. Saksena, S. D. Emr, SnapShot: The ESCRT machinery. *Cell* **137**, 182–182.e1 (2009).
- T. Tian, Y. Wang, H. Wang, Z. Zhu, Z. Xiao, Visualizing of the cellular uptake and intracellular trafficking of exosomes by live-cell microscopy. *J. Cell. Biochem.* **111**, 488–496 (2010).
- S. Pluchino, J. A. Smith, Explicating exosomes: Reclassifying the rising stars of intercellular communication. *Cell* **177**, 225–227 (2019).
- V. D. Atayde, K. Hassani, A. da Silva Lira Filho, A. R. Borges, A. Adhikari, C. Martel, M. Olivier, Leishmania exosomes and other virulence factors: Impact on innate immune response and macrophage functions. *Cell. Immunol.* **309**, 7–18 (2016).
- M. L. Broekman, S. L. N. Maas, E. R. Abels, T. R. Mempel, A. M. Krichevsky, X. O. Breakefield, Multidimensional communication in the microenvirons of glioblastoma. *Nat. Rev. Neurol.* **14**, 482–495 (2018).
- Y.-M. Wang, M. P. Trinh, Y. Zheng, K. Guo, L. A. Jimenez, W. Zhong, Analysis of circulating non-coding RNAs in a non-invasive and cost-effective manner. *Trends Analyt. Chem.* **117**, 242–262 (2019).
- J. S. Schorey, Y. Cheng, P. P. Singh, V. L. Smith, Exosomes and other extracellular vesicles in host-pathogen interactions. *EMBO Rep.* **16**, 24–43 (2015).
- R. Kalluri, V. S. LeBleu, The biology, function, and biomedical applications of exosomes. *Science* **367**, eaau6977 (2020).
- G. van Niel, G. D'Angelo, G. Raposo, Shedding light on the cell biology of extracellular vesicles. *Nat. Rev. Mol. Cell Biol.* **19**, 213–228 (2018).
- S. L. N. Maas, X. O. Breakefield, A. M. Weaver, Extracellular vesicles: Unique intercellular delivery vehicles. *Trends Cell Biol.* **27**, 172–188 (2017).
- S. Wang, A. Khan, R. Huang, S. Ye, K. Di, T. Xiong, Z. Li, Recent advances in single extracellular vesicle detection methods. *Biosens. Bioelectron.* **154**, 112056 (2020).

25. F. Coccozza, E. Grisard, L. Martin-Jaular, M. Mathieu, C. Théry, Snapshot: Extracellular vesicles. *Cell* **182**, 262–262.e1 (2020).
26. P. Zhang, X. Zhou, Y. Zeng, Multiplexed immunophenotyping of circulating exosomes on nano-engineered ExoProfile chip towards early diagnosis of cancer. *Chem. Sci.* **10**, 5495–5504 (2019).
27. S. Ferguson, R. Weissleder, Modeling EV kinetics for use in early cancer detection. *Adv. Biosyst.* **4**, e1900305 (2020).
28. S. Ferguson, K. S. Yang, P. Zelga, A. S. Liss, J. C. T. Carlson, C. F. Del Castillo, R. Weissleder, Single-EV analysis (sEVA) of mutated proteins allows detection of stage 1 pancreatic cancer. *Sci. Adv.* **8**, eabm3453 (2022).
29. A. Morales-Kastresana, T. A. Musich, J. A. Welsh, W. Telford, T. Demberg, J. C. S. Wood, M. Bigos, C. D. Ross, A. Kachynski, A. Dean, E. J. Felton, J. Van Dyke, J. Tigges, V. Toxavidis, D. R. Parks, W. R. Overton, A. H. Kesarwala, G. J. Freeman, A. Rosner, S. P. Perfetto, L. Pasquet, M. Terabe, K. McKinnon, V. Kapoor, J. B. Trepel, A. Puri, H. Kobayashi, B. Yung, X. Chen, P. Guion, P. Choyke, S. J. Knox, I. Ghiran, M. Robert-Guroff, J. A. Berzofsky, J. C. Jones, High-fidelity detection and sorting of nanoscale vesicles in viral disease and cancer. *J. Extracell. Vesicles* **8**, 1597603 (2019).
30. M. S. Panagopoulou, A. W. Wark, D. J. S. Birch, C. D. Gregory, Phenotypic analysis of extracellular vesicles: A review on the applications of fluorescence. *J. Extracell. Vesicles* **9**, 1710020 (2020).
31. Y. Tian, M. Gong, Y. Hu, H. Liu, W. Zhang, M. Zhang, X. Hu, D. Aubert, S. Zhu, L. Wu, X. Yan, Quality and efficiency assessment of six extracellular vesicle isolation methods by nano-flow cytometry. *J. Extracell. Vesicles* **9**, 1697028 (2020).
32. J. A. Welsh, E. Van Der Pol, G. J. A. Arkesteijn, M. Bremer, A. Brisson, F. Coumans, F. Dignat-George, E. Duggan, I. Ghiran, B. Giebel, A. Goergens, A. Hendrix, R. Lacroix, J. Lannigan, S. F. W. M. Libregts, E. Lozano-Andres, A. Moraleskastresana, S. Robert, L. De Rond, T. Tertel, J. Tigges, O. De Wever, X. Yan, R. Nieuwland, M. H. M. Wauben, J. P. Nolan, J. C. Jones, MIFlowCyt-EV: A framework for standardized reporting of extracellular vesicle flow cytometry experiments. *J. Extracell. Vesicles* **9**, 1713526 (2020).
33. Z. Nizamudeen, R. Markus, R. Lodge, C. Parmenter, M. Platt, L. Chakrabarti, V. Sottile, Rapid and accurate analysis of stem cell-derived extracellular vesicles with super resolution microscopy and live imaging. *Biochim. Biophys. Acta Mol. Cell Res.* **1865**, 1891–1900 (2018).
34. R. P. McNamara, Y. Zhou, A. B. Eason, J. T. Landis, M. G. Chambers, S. Willcox, T. A. Peterson, B. Schouest, N. J. Maness, A. G. MacLean, L. M. Costantini, J. D. Griffith, D. P. Dittmer, Imaging of surface microdomains on individual extracellular vesicles in 3-D. *J. Extracell. Vesicles* **11**, e12191 (2022).
35. D. Wu, J. Yan, X. Shen, Y. Sun, M. Thulin, Y. Cai, L. Wik, Q. Shen, J. Oelrich, X. Qian, K. L. Dubois, K. G. Ronquist, M. Nilsson, U. Landegren, M. Kamali-Moghadam, Profiling surface proteins on individual exosomes using a proximity barcoding assay. *Nat. Commun.* **10**, 3854 (2019).
36. K. Lee, K. Fraser, B. Ghaddar, K. Yang, E. Kim, L. Balaj, E. A. Chiocca, X. O. Breakefield, H. Lee, R. Weissleder, Multiplexed profiling of single extracellular vesicles. *ACS Nano* **12**, 494–503 (2018).
37. J. Min, T. Son, J.-S. Hong, P. S. Cheah, A. Wegemann, K. Murlidharan, R. Weissleder, H. Lee, H. Im, Plasmon-enhanced biosensing for multiplexed profiling of extracellular vesicles. *Adv. Biosys.* **4**, e2000003 (2020).
38. M. H. Jeong, T. Son, Y. K. Tae, C. H. Park, H. S. Lee, M. J. Chung, J. Y. Park, C. M. Castro, R. Weissleder, J. H. Jo, S. Bang, H. Im, Plasmon-enhanced single extracellular vesicle analysis for cholangiocarcinoma diagnosis. *Adv. Sci.(Weinh)* **10**, e2205148 (2023).
39. S. Wang, W. Zheng, R. Wang, L. Zhang, L. Yang, T. Wang, J. G. Saliba, S. Chandra, C.-Z. Li, C. J. Lyon, T. Y. Hu, Monocrystalline labeling enables stable plasmonic enhancement for isolation-free extracellular vesicle analysis. *Small* **19**, e2204298 (2023).
40. P. Wei, F. Wu, B. Kang, X. Sun, F. Heskia, A. Pachot, J. Liang, D. Li, Plasma extracellular vesicles detected by Single Molecule array technology as a liquid biopsy for colorectal cancer. *J. Extracell. Vesicles* **9**, 1809765 (2020).
41. D. He, H. Wang, S. L. Ho, H. N. Chan, L. Hai, X. He, K. Wang, H. W. Li, Total internal reflection-based single-vesicle in situ quantitative and stoichiometric analysis of tumor-derived exosomal microRNAs for diagnosis and treatment monitoring. *Theranostics* **9**, 4494–4507 (2019).
42. J. Zhou, Z. Wu, J. Hu, D. Yang, X. Chen, Q. Wang, J. Liu, M. Dou, W. Peng, Y. Wu, W. Wang, C. Xie, M. Wang, Y. Song, H. Zeng, C. Bai, High-throughput single-EV liquid biopsy: Rapid, simultaneous, and multiplexed detection of nucleic acids, proteins, and their combinations. *Sci. Adv.* **6**, 4494–4507 (2020).
43. L. Ayers, R. Pink, D. R. F. Carter, R. Nieuwland, Clinical requirements for extracellular vesicle assays. *J. Extracell. Vesicles* **8**, 1593755 (2019).
44. M. Cao, R. Isaac, W. Yan, X. Ruan, L. Jiang, Y. Wan, J. Wang, E. Wang, C. Caron, S. Neben, D. Drygin, D. P. Pizzo, X. Wu, X. Liu, A. R. Chin, M. Y. Fong, Z. Gao, K. Guo, O. Fadare, R. B. Schwab, Y. Yuan, S. E. Yost, J. Mortimer, W. Zhong, W. Ying, J. D. Bui, D. D. Sears, J. M. Olefsky, S. E. Wang, Cancer-cell-secreted extracellular vesicles suppress insulin secretion through miR-122 to impair systemic glucose homeostasis and contribute to tumour growth. *Nat. Cell Biol.* **24**, 954–967 (2022).
45. M. Y. Fong, W. Zhou, L. Liu, A. Y. Alontaga, M. Chandra, J. Ashby, A. Chow, S. T. F. O'Connor, S. Li, A. R. Chin, G. Somlo, M. Palomares, Z. Li, J. R. Tremblay, A. Tsuyada, G. Sun, M. A. Reid, X. Wu, P. Swiderski, X. Ren, Y. Shi, M. Kong, W. Zhong, Y. Chen, S. E. Wang, Breast-cancer-secreted miR-122 reprograms glucose metabolism in premetastatic niche to promote metastasis. *Nat. Cell Biol.* **17**, 183–194 (2015).
46. B. Li, Y. Cao, M. Sun, H. Feng, Expression, regulation, and function of exosome-derived miRNAs in cancer progression and therapy. *FASEB J.* **35**, e21916 (2021).
47. S. Gurung, D. Perocheau, L. Touramanidou, J. Baruteau, The exosome journey: From biogenesis to uptake and intracellular signalling. *Cell Commun. Signal* **19**, 47 (2021).
48. D. Daassi, K. M. Mahoney, G. J. Freeman, The importance of exosomal PDL1 in tumour immune evasion. *Nat. Rev. Immunol.* **20**, 209–215 (2020).
49. H. Chen, L. Zhao, Y. Meng, X. Qian, Y. Fan, Q. Zhang, C. Wang, F. Lin, B. Chen, L. Xu, W. Huang, J. Chen, X. Wang, Sulfonylurea receptor 1-expressing cancer cells induce cancer-associated fibroblasts to promote non-small cell lung cancer progression. *Cancer Lett.* **536**, 215611 (2022).
50. S. Du, J. Qian, S. Tan, W. Li, P. Liu, J. Zhao, Y. Zeng, L. Xu, Z. Wang, J. Cai, Tumor cell-derived exosomes deliver TIE2 protein to macrophages to promote angiogenesis in cervical cancer. *Cancer Lett.* **529**, 168–179 (2022).
51. L. Santangelo, G. Giurato, C. Cicchini, C. Montaldo, C. Mancone, R. Tarallo, C. Battistelli, T. Alonzi, A. Weisz, M. Tripodi, The RNA-Binding protein SYNCRIP is a component of the hepatocyte exosomal machinery controlling MicroRNA sorting. *Cell Rep.* **17**, 799–808 (2016).
52. Y. Teng, Y. Ren, X. Hu, J. Mu, A. Samykutty, X. Zhuang, Z. Deng, A. Kumar, L. Zhang, M. L. Merchant, J. Yan, D. M. Miller, H.-G. Zhang, MVP-mediated exosomal sorting of miR-193a promotes colon cancer progression. *Nat. Commun.* **8**, 14448 (2017).
53. M. M. Temoche-Diaz, M. J. Shurtleff, R. M. Nottingham, J. Yao, R. P. Fadadu, A. M. Lambowitz, R. Schekman, Distinct mechanisms of microRNA sorting into cancer cell-derived extracellular vesicle subtypes. *eLife* **8**, e47544 (2019).
54. K. Jerabkova-Roda, A. Dupas, N. Osmani, V. Hyenne, J. G. Goetz, Circulating extracellular vesicles and tumor cells: Sticky partners in metastasis. *Trends Cancer* **8**, 799–805 (2022).
55. K. Ekstrom, R. Crescitelli, H. I. Petrusson, J. Johansson, C. Lasser, R. Olofsson Bagge, Characterization of surface markers on extracellular vesicles isolated from lymphatic exudate from patients with breast cancer. *BMC Cancer* **22**, 50 (2022).
56. F. Tian, S. Zhang, C. Liu, Z. Han, Y. Liu, J. Deng, Y. Li, X. Wu, L. Cai, L. Qin, Q. Chen, Y. Yuan, Y. Liu, Y. Cong, B. Ding, Z. Jiang, J. Sun, Protein analysis of extracellular vesicles to monitor and predict therapeutic response in metastatic breast cancer. *Nat. Commun.* **12**, 2536 (2021).
57. M. A. Hollingsworth, B. J. Swanson, Mucins in cancer: Protection and control of the cell surface. *Nat. Rev. Cancer* **4**, 45–60 (2004).
58. K. Guo, Z. Li, A. Win, R. Corea, G. B. Adkins, X. Cui, D. Yan, M. Cao, S. E. Wang, W. Zhong, Calibration-free analysis of surface proteins on single extracellular vesicles enabled by DNA nanostructure. *Biosens. Bioelectron.* **192**, 113502 (2021).
59. M. Abolghasemi, S. S. Tehrani, T. Yousefi, A. Karimian, A. Mahmoodpoor, A. Ghamari, F. Jadidi-Niaragh, M. Yousefi, H. S. Kafil, M. Bastami, M. Edalati, S. Eyvazi, M. Naghizadeh, N. Targhazeh, B. Yousefi, A. Safa, M. Majidinia, V. Rameshkhnia, MicroRNAs in breast cancer: Roles, functions, and mechanism of actions. *J. Cell. Physiol.* **235**, 5008–5029 (2020).
60. M. H. Li, X. Zou, T. S. Xia, T. S. Wang, P. Liu, X. Zhou, S. Wang, W. Zhu, A five-miRNA panel in plasma was identified for breast cancer diagnosis. *Cancer Med.* **8**, 7006–7017 (2019).
61. W. Shen, K. Guo, G. B. Adkins, Q. Jiang, Y. Liu, S. Sedano, Y. Duan, W. Yan, S. E. Wang, K. Bergersen, D. Worth, E. H. Wilson, W. Zhong, A single extracellular vesicle (EV) flow cytometry approach to reveal EV heterogeneity. *Angew. Chem. Int. Ed.* **57**, 15675–15680 (2018).
62. Z. W. Li, J. B. Jin, F. Yang, N. N. Song, Y. D. Yin, Coupling magnetic and plasmonic anisotropy in hybrid nanorods for mechanochromic responses. *Nat. Commun.* **11**, 2883 (2020).
63. M. P. Gupta, S. Tandalam, S. Ostrager, A. S. Lever, A. R. Fung, D. D. Hurley, G. B. Alegre, J. E. Espinal, H. L. Remmel, S. Mukherjee, B. M. Levine, R. P. Robins, H. Molina, B. D. Dill, C. M. Kenific, T. Tuschi, D. Lyden, D. J. D'Amico, J. T. G. Pena, Non-reversible tissue fixation retains extracellular vesicles for in situ imaging. *Nat. Methods* **16**, 1269–1273 (2019).
64. J. T. G. Pena, C. Sohn-Lee, S. H. Rouhanifard, J. Ludwig, M. Hafner, A. Mihailovic, C. Lim, D. Holoch, P. Berninger, M. Zavolan, T. Tuschi, miRNA in situ hybridization in formaldehyde and EDC-fixed tissues. *Nat. Methods* **6**, 139–141 (2009).
65. J. D. Spitzberg, S. Ferguson, K. S. Yang, H. M. Peterson, J. C. T. Carlson, R. Weissleder, Multiplexed analysis of EV reveals specific biomarker composition with diagnostic impact. *Nat. Commun.* **14**, 1239 (2023).
66. L. Cui, R. X. Peng, C. F. Zeng, J. L. Zhang, Y. Z. Lu, L. Zhu, M. J. Huang, Q. H. Tian, Y. L. Song, C. Y. Yang, A general strategy for detection of tumor-derived extracellular vesicle microRNAs using aptamer-mediated vesicle fusion. *Nano Today* **46**, 101599 (2022).
67. D. L. Holliday, V. Speirs, Choosing the right cell line for breast cancer research. *Breast Cancer Res.* **13**, 215 (2011).

68. R. M. Neve, K. Chin, J. Fridlyand, J. Yeh, F. L. Baehner, T. Fevr, et al., A collection of breast cancer cell lines for the study of functionally distinct cancer subtypes. *Cancer Cell* **10**, 515–527 (2006).
69. J. Chen, A. D. Gill, B. L. Hickey, Z. Gao, X. Cui, R. J. Hooley, W. Zhong, Machine learning aids classification and discrimination of noncanonical DNA folding motifs by an arrayed host:Guest sensing system. *J. Am. Chem. Soc.* **143**, 12791–12799 (2021).
70. J. Chen, B. L. Hickey, Z. Gao, A. A. P. Raz, R. J. Hooley, W. Zhong, Sensing base modifications in non-canonically folded DNA with an optimized host:Guest sensing array. *ACS Sens.* **7**, 2164–2169 (2022).
71. D. K. Jeppesen, A. M. Fenix, J. L. Franklin, J. N. Higginbotham, Q. Zhang, L. J. Zimmerman, D. C. Liebler, J. Ping, Q. Liu, R. Evans, W. H. Fissell, J. G. Patton, L. H. Rome, D. T. Burnette, R. J. Coffey, Reassessment of exosome composition. *Cell* **177**, 428–445.e18 (2019).
72. K. B. Johnsen, J. M. Gudbergsson, T. L. Andresen, J. B. Simonsen, What is the blood concentration of extracellular vesicles? Implications for the use of extracellular vesicles as blood-borne biomarkers of cancer. *Biochim. Biophys. Acta Rev. Cancer* **1871**, 109–116 (2019).
73. O. Ruhen, K. Meehan, Tumor-derived extracellular vesicles as a novel source of protein biomarkers for cancer diagnosis and monitoring. *Proteomics* **19**, e1800155 (2019).
74. Z. Zhao, J. Fan, Y.-M. S. Hsu, C. J. Lyon, B. Ning, T. Y. Hu, Extracellular vesicles as cancer liquid biopsies: From discovery, validation, to clinical application. *Lab Chip* **19**, 1114–1140 (2019).
75. A. R. Chin, S. E. Wang, Cancer-derived extracellular vesicles: The 'soil conditioner' in breast cancer metastasis? *Cancer Metastasis Rev.* **35**, 669–676 (2016).
76. S. J. Kim, J. Y. Shin, K. D. Lee, Y. K. Bae, K. W. Sung, S. J. Nam, K. H. Chun, MicroRNA let-7a suppresses breast cancer cell migration and invasion through downregulation of C-C chemokine receptor type 7. *Breast Cancer Res.* **14**, R14 (2012).
77. F. J. Sheedy, Turning 21: Induction of miR-21 as a Key Switch in the Inflammatory Response. *Front. Immunol.* **29**, 19 (2015).
78. Y. Yarden, Biology of HER2 and its importance in breast cancer. *Oncology* **61**, 1–13 (2001).

Acknowledgments: We thank I. Lee at the Central Facility for Advanced Microscopy and Microanalysis (CFAMM) at UC Riverside with the assistance of SEM. **Funding:** This work was supported by UCR's Extramural Funding Opportunity Preparation Award (EFOPA) (W.Z.), City of Hope–UC Riverside Biomedical Research Initiative (CUBRI) Award (W.Z.), National Institutes of Health grant R21DA053496 (W.Z.), National Institutes of Health grant R01CA266486 (S.E.W.), and The Engineering Research Centers Program of the National Science Foundation under NSF Cooperative Agreement No. 1941543 (Y.Y.). **Author contributions:** Conceptualization: W.Z. Methodology: Z.L., K.G., and M.C. Investigation: Z.L. and K.G. Visualization: Z.L. and K.G. Supervision: W.Z. Writing—original draft: W.Z. and Z.L. Writing—review and editing: Z.L. and K.G. Material synthesis: Z.L., Z.Y., and Y.Y. Cell lines and EV preparation: Z.G. Statistical analysis: Z.L. and J.C. Marker selection and discussion: S.E.W. **Competing interests:** The authors declare that they have no competing interests. **Data and materials availability:** All data needed to evaluate the conclusions in the paper are present in the paper and/or the Supplementary Materials.

Submitted 27 March 2023
Accepted 25 January 2024
Published 28 February 2024
10.1126/sciadv.adh8689